frontiers | Frontiers in Chemistry

TYPE Original Research
PUBLISHED 25 September 2024
DOI 10.3389/fchem.2024.1469804

OPEN ACCESS

EDITED BY
Hairong Xue,
Zhengzhou University, China

REVIEWED BY
Gong Hao,
Nanjing Forestry University, China
Wen Luo,
Shanghai University, China

*CORRESPONDENCE
Biswanath Das,
biswanath.das@su.se

†These authors have contributed equally to this work

RECEIVED 24 July 2024
ACCEPTED 12 September 2024
PUBLISHED 25 September 2024

CITATION
Toledo-Carrillo EA, García-Rodríguez M, Morallón E, Cazorla-Amorós D, Ye F, Kundi V, Kumar PV, Verho O, Dutta J, Åkermark B and Das B (2024) Co-complexes on modified graphite surface for steady green hydrogen production from water at neutral pH. *Front. Chem.* 12:1469804. doi: 10.3389/fchem.2024.1469804

Co-complexes on modified graphite surface for steady green hydrogen production from water at neutral pH

Esteban A. Toledo-Carrillo[1†], Mario García-Rodríguez[2†], Emilia Morallón[2], Diego Cazorla-Amorós[3], Fei Ye[1], Varun Kundi[4], Priyank V. Kumar[4], Oscar Verho[5], Joydeep Dutta[1], Bjorn Åkermark[6] and Biswanath Das[6]*

[1]Department of Applied Physics, KTH Royal Institute of Technology, Stockholm, Sweden, [2]Departamento de Química Física e Instituto Universitario de Materiales, Universidad de Alicante, Alicante, Spain, [3]Departamento de Química Inorgánica e Instituto Universitario de Materiales, Universidad de Alicante, Alicante, Spain, [4]School of Chemical Engineering, University of New South Wales, Sydney, NSW, Australia, [5]Department of Medicinal Chemistry, Biomediciniskt Centrum BMC, Uppsala University, Uppsala, Sweden, [6]Department of Organic Chemistry, Arrhenius Laboratory Stockholm University, Stockholm, Sweden

Green hydrogen production from water is one attractive route to non-fossil fuel and a potential source of clean energy. Hydrogen is not only a zero-carbon energy source but can also be utilized as an efficient storage of electrical energy generated through various other sources, such as wind and solar. Cost-effective and environmentally benign direct hydrogen production through neutral water (~pH 7) reduction is particularly challenging due to the low concentration of protons. There is currently a major need for easy-to-prepare, robust, as well as active electrode materials. Herein we report three new molecular electrodes that were prepared by anchoring commercially available, and environmentally benign cobalt-containing electrocatalysts with three different ligand frameworks (porphyrin, phthalocyanine, and corrin) on a structurally modified graphite foil surface. Under the studied reaction conditions (over 7 h at 22°C), the electrode with Co-porphyrin is the most efficient for the water reduction with starting ~740 mV onset potential (OP) (vs. RHE, current density 2.5 mA/cm^2) and a Tafel slope (TS) of 103 mV/dec. It is followed by the molecular electrodes having Co-phthalocyanine [825 mV (OP), 138 mV/dec (TS)] and Vitamin-B_{12} (Co-corrin moiety) [830 mV (OP), 194 mv/dec (TS)]. A clear time-dependent improvement (>200 mV over 3 h) in the H_2 production overpotential with the Co-porphyrin-containing cathode was observed. This is attributed to the activation due to water coordination to the Co-center. A long-term chronopotentiometric stability test shows a steady production of hydrogen from all three cathode surfaces throughout seven hours, confirmed using an H_2 needle sensor. At a current density of 10 mA/cm^2, the Co-porphyrin-containing electrode showed a TOF value of 0.45 s^{-1} at 870 mV vs. RHE, whereas the Co-phthalocyanine and Vitamin-B_{12}-containing electrodes showed 0.37 and 0.4 s^{-1} at 1.22 V and 1.15 V (vs. RHE), respectively.

KEYWORDS

green hydrogen, water reduction, molecular electrodes, cobalt, sustainable energy, electrocatalysis

1 Introduction

Efficient electrochemical production of hydrogen (H_2) from water under mild conditions at a close to neutral pH is vital from the perspective of sustainable green energy production (Kandemir et al., 2016; Xie et al., 2019; Hoque et al., 2020; Shiva Kumar and Lim, 2022; Das et al., 2023; Zainal et al., 2024).

The state-of-the-art catalysts for the Hydrogen Evolution Reaction (HER) are Pt-based, which increases the overall cost of the system due to the scarcity of noble metals like Pt (Faber and Jin, 2014; Toledo-Carrillo et al., 2024). Thus, many studies have been conducted for searching of novel low-cost electrocatalysts, based on a variety of non-precious earth abundant transition metals, including Fe, Co, Ni, Cu, Mn, and their complexes (Sun et al., 2020; Wang et al., 2020; Makhado et al., 2021). Manganese-, iron- and cobalt-based transition metal oxides have been found to have high electrocatalytic activity because of the existence of various oxidations states, high conductivity, and excellent structural durability (Moni et al., 2017; Sun et al., 2017; Zhu et al., 2018). Nickel transition metal has also been reported to be active for HER; Li M. et al. (2019) applied ZnO nanorods supported nickel foam (NF) as the template to fabricate $Ni_3ZnC_{0.7}$/NCNT (NCNT: nitrogen-doped carbon nanotube) arrays for water splitting; and Elakkiya et al. (2019) fabricated a flower-like nanoporous-$NiCo_2O_4$ material as electrocatalyst for the water splitting in alkaline media, which displayed a high mass activity with low overpotentials, and small Tafel slopes due to its unique surface and electronic band structure with abundant active sites and porosity, electrochemical active surface area, rapid electron transfer and structural durability. Other elements such as Mo (Li R. et al., 2019), Ni-Co (Zhang et al., 2019), Ni-Co-Mo (Hu et al., 2019) and Mo-Mn (Gong et al., 2019) alloys, and Ir-Ag (Zhu et al., 2019) nanotubes show also promising results. Furthermore, to expose more active sites and increase the electric conductivity, it is an effective way to coat the electrocatalysts on the three-dimensional (3D) conductive support. For instance, Xu et al. (2019) successfully anchored the integrated hybrid electrocatalyst of $NiFe_2O_4$ nanoparticles directly on the vertically aligned carbon nanotubes showing enhanced electrocatalytic performance. This is attributed to the synergistic effect raising from the interaction of metal nanoparticles and the carbon nanotubes.

The importance of the conductive support is highlighted in a number of reports utilizing cobalt-containing molecular electrocatalysts. (McAlpin et al., 2010; Kim et al., 2015; Kandemir et al., 2016; Yang et al., 2017; Das et al., 2022). For instance, vitamin B_{12} (VB_{12}), a cobalt-containing naturally abundant catalyst, has been successfully tested for several electrocatalytic reactions, including electrochemical processes such as water oxidation, proton reduction, and carbon dioxide reduction (Giedyk et al., 2015; Jia et al., 2020). Although the redox-active corrin-ligand framework in VB_{12} allows the cobalt center to readily shuttle between +3 and +1 oxidation states, it remains challenging to modify the substituents on the ring. Small molecules with simpler ligand frameworks as alternatives allow easier structural modification for stepwise improvement, e.g., metal complexes with porphyrins and phthalocyanines (Kärkäs et al., 2014; Das et al., 2019). These complexes with various electron-donating or withdrawing groups in the periphery have been studied due to their easy handling and electrocatalytic response.

Molecular electrocatalysis allows detailed structural understanding, modification, and optimization which is hard to obtain from metal oxides-assisted electrocatalytic processes due to the comparatively lesser understanding of the structure and morphology of the latter (Copéret et al., 2003). However, molecular systems undergo deactivation due to decomposition and polymerization in solution. Metal-leaching and/or copolymerization are other common disadvantages of molecular inorganic catalysts. This can be avoided by anchoring them on the modified solid conductive surface through a suitable linker (Hoque et al., 2020; Gil-Sepulcre et al., 2021; Ventosa et al., 2021; Das et al., 2023). These molecular electrodes allow structural understanding at the molecular level as well as provide higher stability of the catalysts. Herein we present three cobalt-containing electrocatalysts with corrin (vitamin B_{12}), porphyrin, and phthalocyanine ligand frameworks (Figure 1) which are anchored on pyridine-modified graphite foil (G_PF), and their electrocatalytic hydrogen production performance at the neutral pH (pH 7.1, 0.1 M phosphate buffer) conditions was investigated. From the cumulative electrocatalytic results, it is clear that the Co-porphyrin system on the modified graphite surface is by far the best electrode for hydrogen production (with −743 mV vs RHE) through direct water reduction in terms of onset potential (−740 mV overpotential at 2.5 mA/cm^2) but also in terms of stability, showing a stable potential for up to seven hours at 10 mA/cm^2.

The results are supported by X-ray photoelectron spectroscopy (XPS), cyclic voltammetry (CV), linear sweep voltammetry (LSV), electrochemical impedance spectroscopy (EIS), UV-Vis spectroscopy, transmission electron microscopy (TEM) and scanning electron microscopy (SEM).

2 Results and discussion

2.1 Synthesis

To covalently link the electrocatalysts on conductive graphite support, surface modification was done utilizing a diazotization reaction involving 4-(2-aminoethyl) pyridine, isoamyl nitrite, tetrafluoro boric acid, and acetic acid (see Supplementary Material for detailed procedure) (Das et al., 2022; Das et al., 2023). This resulted in a pyridine-modified graphite foil (G_PF) that allows free pyridyl groups to form covalent bonding interactions with the molecular electrocatalysts while being linked to the graphite surface through a -CH_2-CH_2- unit. This technique of structural modification of the carbon cloth is tested and optimized for large-scale production which results in a minimal amount of waste (Das et al., 2023).

Three separate 10 mL 0.5 mM solutions (Water: Ethanol 1:4) of cobalt (II) tetrakis (4-methoxyphenyl) -porphyrin, cobalt (II) phthalocyanine, and vitamin B_{12} were prepared and degassed with nitrogen for 5 min before using for catalyst anchoring. To covalently attach the electrocatalysts, 2 cm × 2 cm G_PF was immersed into the freshly prepared solutions, and the container was kept at 65°C for a period of 6 h under continuous slow stirring and a nitrogen atmosphere. It was followed by careful collection of the electrodes and washing them with cold water (3 × 1 mL) and acetone (2 × 1 mL) before drying them in a 60°C oven overnight. It

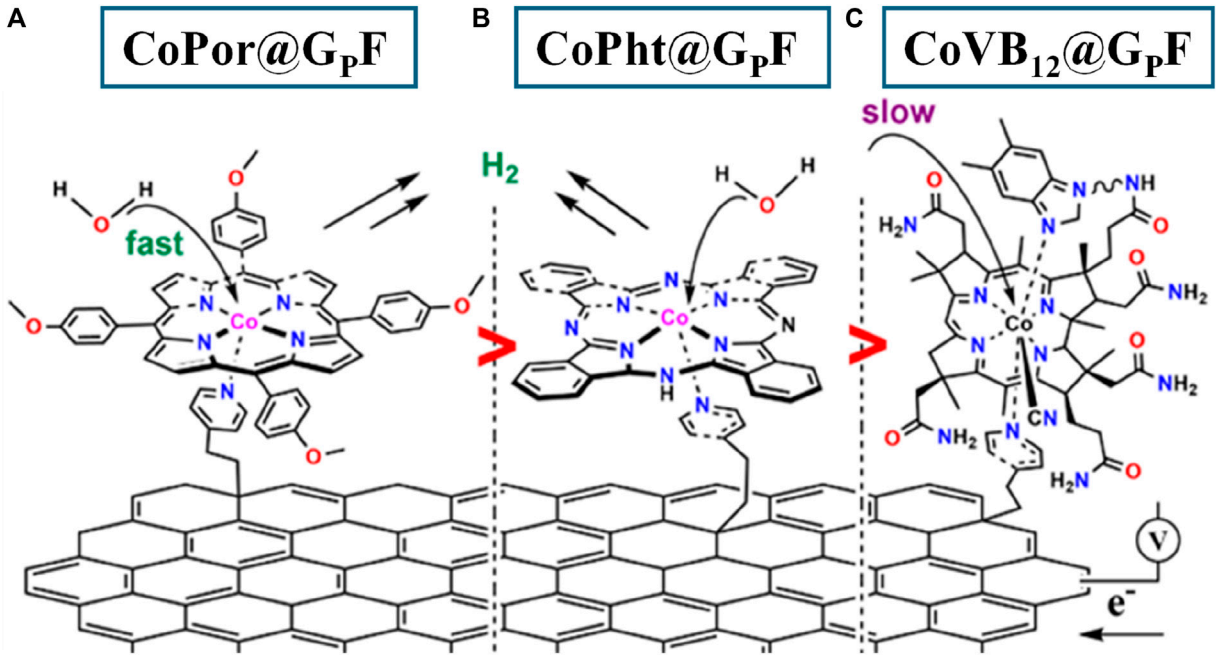

FIGURE 1
Pictorial representation of the electrodes [CoPor@G_PF **(A)**, CoPht@G_PF **(B)**, and $CoVB_{12}$@G_PF **(C)**] that are studied in this project.

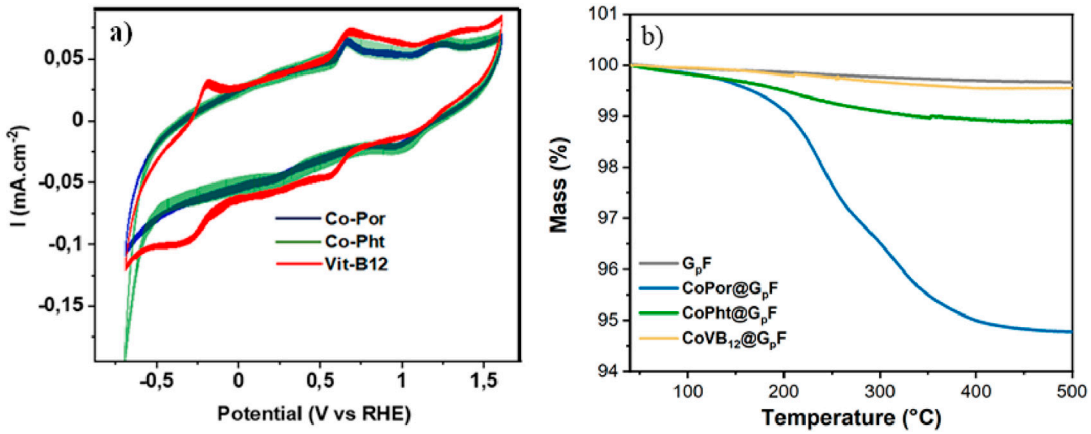

FIGURE 2
(A) Cyclic voltammogram of 1 mM cobalt (II) tetrakis (4-methoxyphenyl) -porphyrin (Co-Por), cobalt (II) phthalocyanine (Co-Pht), and vitamin B_{12} (Co-VB_{12}) in pH 7.1 phosphate buffer (0.1 M) solution. 5 v% of ethanol was added in the case of Co-Por to completely solubilize this sample. **(B)** Thermogravimetric analysis (TGA) of G_PF and all three electrodes CoPor@G_PF, CoPht@G_PF, and $CoVB_{12}$@G_PF.

resulted in the molecular cathodes CoPor@G_PF (Figure 1A), CoPht@G_PF (Figure 1B), and $CoVB_{12}$@G_PF (Figure 1C).

2.2 Characterization

All three molecular catalysts are commercially available with >99% purity and no further purification was performed before anchoring them onto G_PF. The electrochemical responses of CoPor, CoPht, and $CoVB_{12}$ were investigated in pH 7.1 phosphate buffer (Figure 2A) prior to their anchoring to graphite foil. Both Co-Por and Co-Pht showed two quasi-reversible redox waves within the potential range of 0.70 V and 1.25 V whereas Co-VB_{12} showed two well-resolved reversible oxidation waves at around −0.25 and 0.6 V. Co-VB_{12} also showed another oxidation wave at around 1.25 V. Interestingly, Co-Pht showed a sharp water reduction feature at around −0.6 V, which was absent in case of Co-Por and $CoVB_{12}$. The redox peaks can be associated with the redox behavior of the cobalt species and also with oxidation/reduction reactions in the π-system ring to form the corresponding radical (Zagal et al., 1992; Sun et al.,

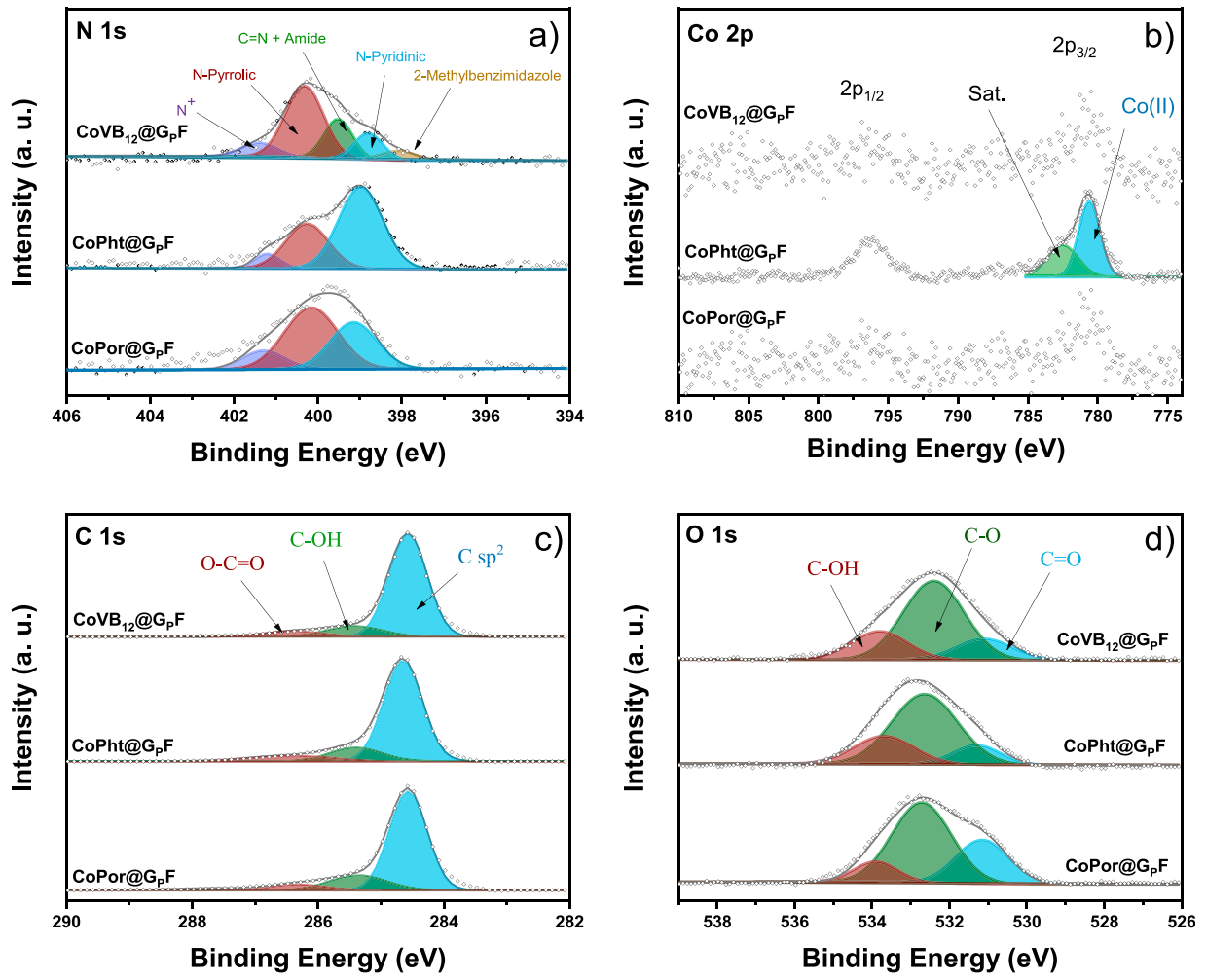

FIGURE 3
XPS analysis [**(A)** N 1S analysis, **(B)** Co 2P analysis, **(C)** C 1S analysis and **(D)** O 1S analysis] of the three electrodes CoPor@G$_P$F (bottom), CoPht@G$_P$F (middle), and CoVB$_{12}$@G$_P$F (top) after the impregnation with 0.1 M phosphate buffer (pH 7.1).

2003; Calabuig-Mompó et al., 2024). Previously reported systems have identified that the molecular catalysts can undergo decomposition upon prolonged electrolysis and might not be reliable in case of prolonged electrocatalysis (Lee et al., 2019). The current study investigates the reactivity of these molecular catalysts after they are anchored to modified graphite foil using covalent bonding through pyridyl units. The electrocatalysis was tested for continuous hydrogen evolution (via water reduction) over a period of seven hours.

The loading of the catalyst on the graphite foil was studied by thermogravimetric analysis (TGA). Figure 2B shows the weight changes in the range between 30°C–500°C. With similar systems a clear weight loss was observed between 200°C–300°C associated to the desorption of the electrocatalyst, as reported previously (Das et al., 2022). The partial weight reduction as compared to the substrate material reveals a loading of 4.9%, 0.9% and 0.2% for CoPor@G$_P$F, CoPht@G$_P$F, and CoVB$_{12}$@G$_P$F, respectively in the current study. This technique reflects a stronger anchor between the G$_P$F and the active phase of the electrocatalyst in the CoPht@G$_P$F and CoVB$_{12}$@G$_P$F samples compared to the CoPor@G$_P$F sample, which presumably has an influence on the electrocatalytic activity (Zhang and Wang, 2021).

The structural identity of CoPor@G$_P$F, CoPht@G$_P$F, and CoVB$_{12}$@G$_P$F were investigated by XPS, SEM, and TEM spectroscopy. XPS analysis was performed before and after exposing the samples to a 0.1 M phosphate buffer electrolyte overnight (Supplementary Figure S1), since it is expected that the species composing the electrocatalyst change upon contact with the electrolyte. The N 1s and O 1s spectra revealed significant differences, but no changes were observed in the C 1s spectrum. The Co 2p spectrum was only defined in the CoPht@G$_P$F sample, but Co 2p presence in the CoPor@G$_P$F and CoVB$_{12}$@G$_P$F samples could be confirmed. The immersion into the electrolyte solution (pH 7.1 phosphate buffer) did not alter the Co 2p spectrum. The main differences resulting from the impregnation with the electrolyte were a 4%–5% increase in O in all samples and a 1% increase in N. Supplementary Tables S1 and S2 show the mass and atomic percentage of all samples.

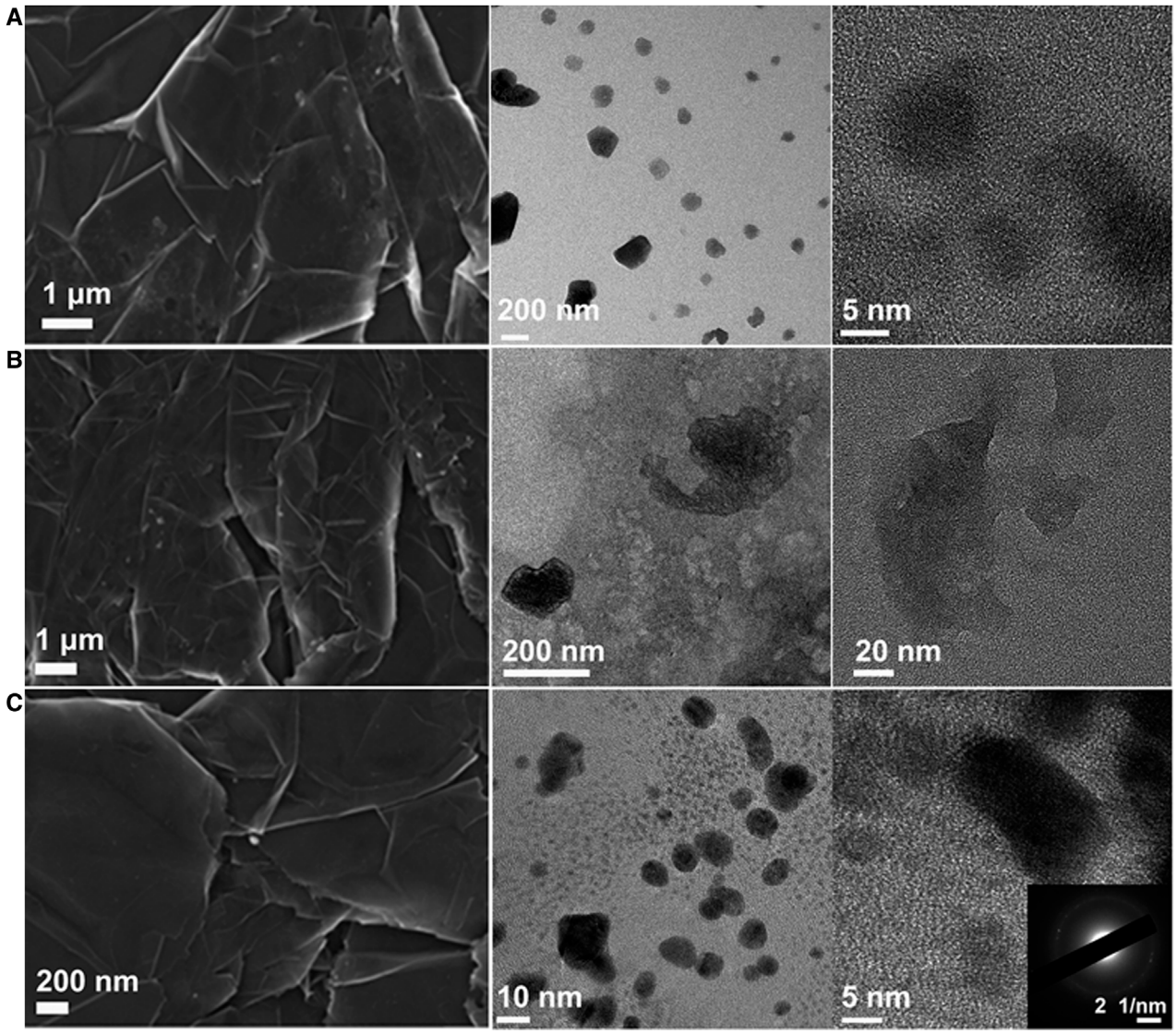

FIGURE 4
SEM images of the active surfaces of the three electrodes: $CoVB_{12}$@G_PF **(A)**, CoPht@G_PF **(B)**, and CoPor@G_PF **(C)**.

To analyse the N and O species in the compounds, the spectra were deconvoluted (Supplementary Table S1 shows the deconvolution parameters applied). Figure 3 displays the deconvolution of the spectra from the impregnated samples, providing a more accurate representation of the catalyst's composition during the reaction. In contrast, the deconvolution of the spectra without immersion can be observed in Supplementary Figure S2. The percentages of the deconvolution of each species can be seen in Supplementary Table S2. A higher concentration of cobalt species from the ligand framework was detected in the CoPht@G_PF sample. Considering that the same treatment was used to anchor the ligand frameworks to the graphite, it is possible to affirm that there is a higher affinity of the phthalocyanine molecules to be anchored to the graphite compared to the porphyrin and VB_{12} molecules. The high-resolution N 1s spectrum of CoPor@G_PF (Figure 3A) reveals three signals. The signal at ~398.9 eV corresponds to the N-pyridine linker to graphite. The signal at ~400.1 eV represents three overlapping possibilities: N-Co bond due to Co addition, N-pyrrole, and N-imine bond resulting from inadequate Co incorporation (Macquet et al., 1978; Mette et al., 2016). The signal at ~401.3 eV is associated with positively charged nitrogen atoms, a common outcome of X-ray radiation during measurement (Alemany-Molina et al., 2022). CoPht@G_PF also has three contributions similar to the CoPor@G_PF sample, with the addition of a new signal from the N-pyridinic-like bond from phthalocyanine (Artyushkova et al., 2008; De Riccardis et al., 2020). $CoVB_{12}$@G_PF shows 5 peaks at ~398.1 eV (2-methylbenzimidazole), ~398.8 eV (N-pyridyl), ~399.5 eV (CN and amide bond), ~400.3 eV (N-Co and N-pyrrolic), and ~401.4 eV (N^+) (Saravanan et al., 2020; Jia et al., 2020).

The high-resolution O 1s spectrum of the three sample types (Figure 3) was deconvoluted and shows three contributions at

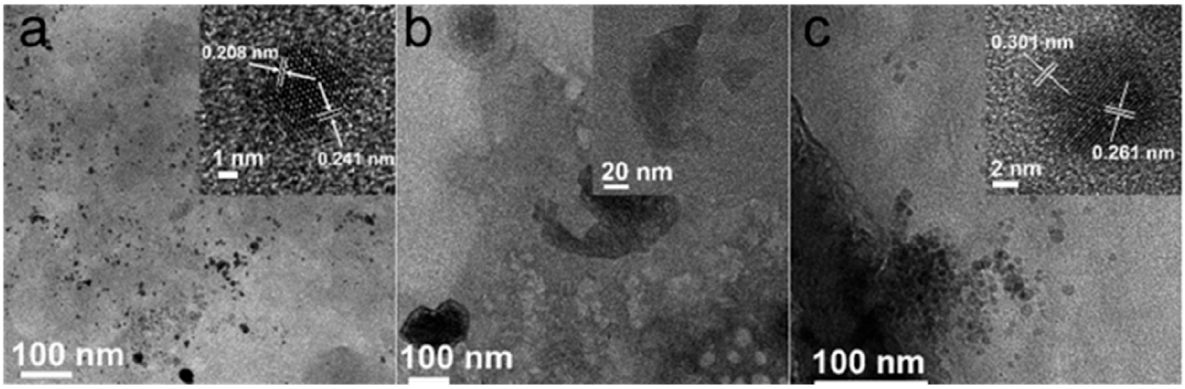

FIGURE 5
TEM phrotographs of **(A)** CoPor@G_PF, **(B)** CoPht@G_PF, and **(C)** CoVB_{12}@G_PF. Insets are higher magnification images, which demonstrate either crystal lattice or enlarged details.

~531.2 eV, ~532.6 eV, and ~533.9 eV, associated with C=O, C-O and C-OH, respectively (Peebles et al., 2017; Saravanan et al., 2020). The electrolyte causes differences with a rise in the C=O ratio (Supplementary Table S3), particularly in the CoPor@G_PF sample that increases by almost 20%. Subsequently, the deconvolution of the Co 2p spectrum for the CoPht@G_PF sample reveals a peak at 780.8 eV, which is associated with the presence of a multilayer of phthalocyanine with adsorbed Co^{2+} on a graphite surface. Additionally, a satellite peak is detected at 782.6 eV, which is attributed to the presence of a sub-monolayer of adsorbed phthalocyanines. This peak has been observed for various combinations of adsorbates and substrates (Gottfried and Marbach, 2009; Petraki et al., 2010; Schmid et al., 2012).

When comparing the samples, a higher contribution of N-pyrrolic groups is observed in the CoPor@G_PF and CoVB_{12}@G_PF samples (accounting for nearly 50%), while in the CoPht@G_PF sample, the predominant group is associated with N-pyridinic groups (approximately 61%). Regarding surface oxygenated groups, all samples show a substantial presence of C-O groups, nearly 60%. However, it is noteworthy that the CoPor@G_PF sample exhibits a higher ratio of C=O species, approaching 30% (Supplementary Table S3).

The electrodes were further studied by scanning electron microscopy (SEM), as depicted in Figure 4. The surface of the pristine graphite substrate presents a wrinkled surface with the clear appearance of graphene layers. The molecular electrode surfaces (after anchoring the electrocatalysts on G_PF), show a similarly smooth surface as the pristine graphite, but with the presence of small aggregates with sizes lower than 100 nm, evidencing the anchoring of the Co-complexes in all three cases, with a well-conserved graphite surface during the synthesis process, which is of great importance to ensure the surface electrical conductivity is conserved as no clear evidence of surface oxidation/exfoliation is observed.

The sample of Co-Por sonicated off from the CoPor@G_PF surface has a size distribution from 1 nm to ca. 15 nm, which can be seen in the TEM picture of Figure 5. We found that smaller-sized particles of Co-Por, typically 1–5 nm in size, exhibited single crystal crystallinity. The crystal lattice was measured as ca. 0.208 nm and 0.241 nm for one particle exampled in a high-resolution TEM image (Figure 5). When the particle size is bigger than ca. 5 nm, the polycrystal structure of the particles was observed, which shows random crystallographic orientations. The broad size distribution and polycrystallinity of the Co-Por particles reflect that the nucleation and crystal growth process of Co-Por when deposited on graphite were not homogeneous.

For Co-Pht sample, the size of the particles is not homogeneous and is bigger than 200 nm. In addition, we did not observe a clear crystal lattice of Co-Pht under TEM (Figure 5B), indicating its low crystallinity. In comparison, Co-Pht had been grown on a KCl {001} substrate in previous work by repeated vacuum deposition and thermal treatment (Yanagiya et al., 2004). As a result, ellipsoid-shaped particles with lengths in micrometer and crystal planes were obtained. The difference in crystallinity should be due to the different conditions of crystal growth.

The Co-VB_{12} sample has a broad size distribution, from around 10 nm to around 200 nm. However, both small and large particles were observed with well-developed single crystal structures. Taking one particle as an example, the lattice spacing was measured as 0.301 nm and 0.261 nm as shown in Figure 5C. This indicates that although the nucleation of Co-VB_{12} might not be homogeneous, the crystal growth had occurred.

2.3 Electrocatalytic H_2-production

The electrocatalytic hydrogen production was evaluated using linear sweep voltammetry (LSV) (Figure 6). For CoPor@G_PF sample, water reduction starts at −743 mV vs. RHE at 2.5 mA/cm^2, which is 85 and 90 mV lower overpotential than that of Co-Pht@G_PF and CoVB_{12}@G_PF, respectively. Although Co-Pht (before being anchored on the graphite surface) showed the best water reduction features in homogeneous conditions, it comes out to be less efficient after anchoring onto G_PF among the samples studied. This can be due to the inefficient charge transfer from the Co-Pht to G_PF, due to the intrinsic structural limitations (El-Khouly et al., 2004). Previously in XPS analysis, a higher concentration of cobalt was detected in CoPht@GPF sample in comparison with the other,

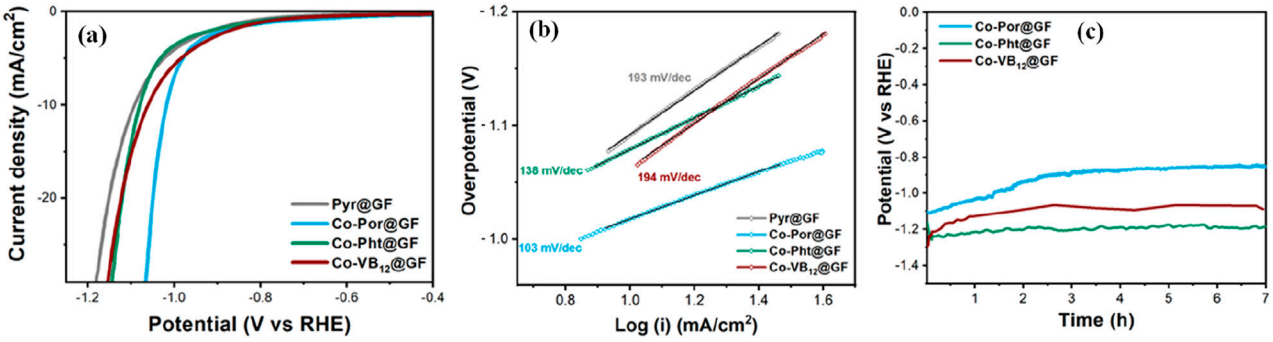

FIGURE 6
LSV measurement **(A)** and corresponding Tafel plots **(B)** for graphite foil (grey), CoPor@G_PF (blue), CoPth@G_PF (green), and CoVB_{12}@G_PF (maroon) in pH 7.1 phosphate buffer (0.1 M) solution purged with N_2. Ag/AgCl (3 M) was used as the reference electrode and the graphite bar was used as the counter electrode. **(C)** Chronopotentiometric response at a current density of 10 mA/cm^2 over a period of 7 h.

possessing a higher ratio of cobalt active sites. Therefore, the active mass of the molecular catalyst framework alone does not dictate electrocatalytic performance. Other factors, such as the anchoring efficiency of the ligand frameworks and the optimal ligand framework-to-graphite ratio, likely play a crucial role. Interestingly, CoVB_{12}@G_PF showed very similar initial water reduction behavior with CoPor@G_PF until −1 V, followed by a clear deviation in the electrochemical response (Figure 6A). CoVB_{12}@G_PF started exhibiting similar current density features as of CoPht@G_PF from −1.12 V onward negative potentials. The steric restrictions and hydrophobic moieties around the Co-center in vitamin B_{12} are expected to be the reasons behind the slow kinetic water reduction features of CoVB_{12}@G_PF (Figure 1 and Supplementary Figure S3) (Giedyk et al., 2015). Moreover, the large size of the VB_{12} does not allow higher catalyst loading on G_PF, resulting lower Co: surface area ratio in CoVB_{12}@G_PF in comparison to that of CoPor@G_PF and CoPht@G_PF, which also impacts in the water reduction reactivity. The better electrocatalytic features and catalyst loading were confirmed by the Tafel plots analysis, which shows a much lower slope value (103 mV/dec) for CoPor@G_PF, followed by CoPht@G_PF and CoVB_{12}@G_PF with values of 138 mV/dec and 194 mv/dec, respectively (Figure 6B). It is widely accepted that the value of the Tafel slope has a close relationship with the HER mechanism (Mahmood et al., 2018). The values obtained from the samples in this work are associated with a Volmer-limited reaction, i.e., the HER limited by the hydrogen adsorption reaction to form M-H_{ads} intermediates (Li F. et al., 2019). All of these three electrodes were tested over a period of 7 h under water reduction conditions. TOF values were calculated (see Supplementary Material) at a current density of 10 mA/cm^2, where steady hydrogen production was confirmed using an H_2 needle sensor. It showed Co-porphyrin containing electrode a TOF value of 0.45 s^{-1} at 870 mV vs. RHE, whereas for Co-phthalocyanine and Vitamin-B_{12} containing electrodes showed TOF value of 0.37 and 0.4 s^{-1} at 1.22 V and 1.15 V (vs. RHE), respectively.

But firstly, in order to understand the potential reasons behind the contradictory behaviour between homogeneous and heterogeneous electrocatalytic tests, we performed impedance measurements (EIS) at different potentials to analyse the different contributions in the electrocatalytic process. Supplementary Figure S4A shows the Nyquist plot, comparing the impedance response of all three electrocatalysts at −1.0 V. The curves were zero-corrected to better visualize the differences on the electrode mechanisms. It is clear that CoPor@G_PF shows the lowest total resistance, as observed by the diameter of the semicircle in Nyquist plot. As expected for CoPor@G_PF sample, at larger overpotential, a reduction in the impedance magnitude was observed, as shown in Supplementary Figure S4B. To further distinguish the different contributions during electrocatalysis the impedance curves were fitted using the equivalent circuit presented in Supplementary Figure S4C. The circuit consist of a two-time constant wherein we proposed a first time constant (CPE1 and R1) is associated to the electrolyte-electrode interface and a second time constant (R2 and CPE2) associated to the interface between the molecular active phase catalyst and the conductive substrate (G_PF). It was not possible to distinguish between different contributions in case of CoVB_{12}@G_PF, but the resistance values for R1 and R2 of CoPht@G_PF and CoPor@G_PF are plotted in Supplementary Figure S4D. From the resistance values it can be observed that CoPht@G_PF shows slightly lower resistance to the charge transfer that is driving the catalytic reaction, well correlating with the results obtained by homogeneous study. On the other hand, a significant difference is observed in R2 values, with lower resistance values for CoPor@G_PF in the overpotential windows tested, which indicates a more favoured conduction of charges through the ligand in case of CoPor@G_PF, compared to CoPht@G_PF. It can be associated to the poor distribution of the molecular catalysts on the surface of the conductive substrate. The large agglomerates make the charge transfer from the conductive support to the metal centre significantly more difficult.

The potential vs. time plot (Figure 6C) clearly shows that CoPor@G_PF improves its reactivity (lower initial potential required to achieve 10 mA/cm^2 current) with time, which is directly related to overpotential. Almost 220 mV improvement of the initial potential was observed for hydrogen evolution reaction (HER) during first 3 h. It is followed by stable current flow and hydrogen production for the next 4 h. The electrolyte solutions after

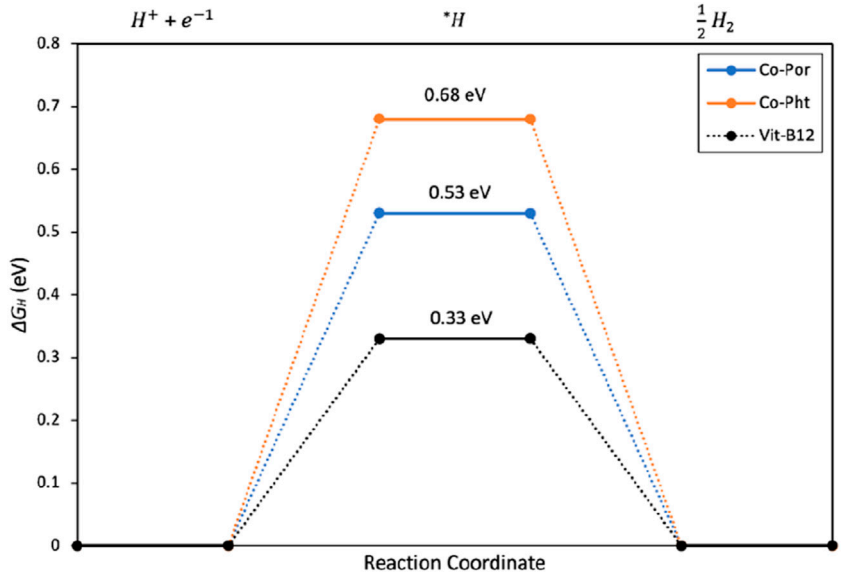

FIGURE 7
DFT calculated Reaction energy diagram for H_2 production using Co-Por, Co-Pht, and Vit-B_{12} as electrocatalysts.

these 7 h electrolysis experiments were investigated by 500 MHz ^{1}H NMR. No evidence of metal leaching or ligand decomposition was observed. The improvement in overpotential can be attributed to the slow coordination of the water molecule and formation of a hydrogen-bonding network around the cobalt center, which is most prominent with CoPor (Okamoto et al., 1975). Water coordinated Co(OH_2)-Por@G_PF is expected to be a more efficient cathode than CoPor@G_PF itself due to easier proton transfer from the activated water molecule at the Co-OH_2 center (Cheng et al., 2022). This activation by water coordination can be corroborated with the highest value of oxygen percentage (O % ~ 9.3%) after the impregnation (Supplementary Table S2) with CoPor@G_PF. Furthermore, the improvement in overpotential could also be related to the presence of reduced Co^0 species, which may emerge under reducing conditions and have been shown to be active in electrochemically relevant reactions (Gupta et al., 2023; Zhang et al., 2023). Electrochemical impedance spectroscopy (EIS) measurements further highlight the better performance of CoPor@G_PF. The superior conductivity observed in this sample facilitates efficient electron transfer to the active Co-OH_2 centers, promoting the HER process. Additionally, transmission electron microscopy (TEM) reveals smaller particle sizes in CoPor@G_PF compared to the other samples. This reduced particle size translates into a larger active surface area, providing more active sites for the HER reaction to occur. Regarding thermal stability, TGA also reveals significant mass losses in CoPor@G_PF between 250°C and 450°C, reaching approximately 5%, while the remaining samples exhibit only around 1% mass loss. This observation confirms the stability of CoPor@G_PF at temperatures below 250°C. The mass loss at higher temperatures is likely associated with the decomposition of weakly anchored porphyrin groups on the graphite surface, potentially contributing to the enhanced electron transfer at the Co-OH_2 centers and also enhancing the electrocatalytic activity.

Although all three electrodes showed stable features under water reduction (hydrogen production) conditions and continuous hydrogen evolution, no such distinct activation features were observed in the case of CoPht@G_PF and CoVB_{12}@G_PF, implying that the formation of Co(OH_2) type species and corresponding improved reactivity is much more prominent in case of CoPor@G_PF which is proving out to be the best water reducing electrode among all three molecular electrodes.

2.4 DFT calculations

We carried out DFT-based free energy calculations of H adsorption at the Co site in the unsupported catalysts to understand the difference in activity between these three Co-based electrocatalysts in H_2 production (Figure 7). The model structures utilized in these calculations are the same as shown in Figure 1 and Supplementary Figure S5. However, for VB_{12}, we removed the -CN moiety and attached H instead. All the structures were geometrically optimized to minimize forces acting on the atoms (see Supplementary Material for details).

It is generally accepted that the free energy changes associated with H adsorption ΔG_{H^*} is a key descriptor for HER catalysts (Ju et al., 2017). A HER catalyst is expected to perform well when the free energy value is close to thermoneutral, i.e., $\Delta G_{H^*} \approx 0$. The results indicate a more optimal hydrogen adsorption for the Vit-B_{12} sample, with a ΔG_{H^*} value of 0.33 eV, followed by the Co-Pht and Co-Por samples, with values of 0.53 and 0.68 eV, respectively. These findings suggest that Vit-B_{12} has the best performance for the hydrogen evolution reaction (HER). However, experimental results have shown that the most electroactive sample is CoPor@G_PF. This discrepancy highlights the influence of molecule adsorption on the graphite sheet, which alters electron transfer, as demonstrated by EIS, thereby modifying the electrocatalytic activity towards HER.

3 Experimental and methods

3.1 Materials

All three catalysts [Co(II)tetrakis (4-methoxyphenyl)-porphyrin, Cobalt (II) phthalocyanine, and Vitamin B_{12}] that are used in this project were commercially available from Merck. They were received as pure (~99%) compounds and used as catalysts without any additional purification. Prior to the catalysts' anchoring, the graphite foil surface was structurally modified following our reported procedure (Das et al., 2023).

3.2 Methods

The surfaces of the pyridine-modified graphite and the modified graphite with Co-complexes catalysts were investigated by scanning electron microscopy (SEM) using Zeiss Gemini Ultra 55 microscope. Transmission electron microscopy (TEM) analysis was performed using an aberration-corrected Themis Z instrument from Thermo Fisher. TEM was operated at 300 kV in Scanning TEM (STEM) mode. The samples were prepared by detaching the catalyst from the graphite substrate by sonication of CoPor@G_PF, CoPht@G_PF, and CoVB_{12}@G_PF in 1 M aqueous KOH for 30 min and dispersed onto a thin carbon support film.

The surface of the electrocatalysts was also examined by X-ray photoelectron spectroscopy (XPS) using a VG-Microtech Multilab 3,000 spectrometer (VG Scientific, Sussex) equipped with a hemispherical electron analyzer with nine channeltrons and an X-ray source with Al radiation. The binding energy of the C 1s peak at 284.6 was taken as an internal standard. Thermogravimetric analysis (TGA) (under N_2 with flow of 5 mL/min in balance and 45 mL/min in furnace) was performed using a TGA Q500 equipment (TA Instrument) under a nitrogen atmosphere to determine weight losses due to the elimination of surface functionalities.

Redox response in the homogeneous condition (Figure 2A) was investigated using a glassy carbon electrode (3 mm diameter) as the working electrode, Ag/AgCl/Cl (sat.) as the reference electrode, and graphite as the counter electrode in 0.1 M phosphate buffer solution (pH 7.1) as electrolyte. Electrocatalytic properties of the designed electrodes were studied in an electrochemical workstation connected to a Potentiostat/Galvanostat/ZRA Gamry Interface 1010E. All the potentials were converted into a reversible hydrogen electrode (RHE) following this equation:

$$E_{RHE} = 0.1976 + E_{Ag|_{AgCl}} + 0.059\,pH$$

The hydrogen evolution reaction (HER) activity was studied by linear sweep voltammetry in the potential window from 0 to −1.4 V vs. RHE at scan rate of 100 mV/s, to determine the overpotentials and Tafel slopes. Electrochemical impedance spectroscopy (EIS) was employed to study the contribution of the structural features of the catalysts. It was conducted under potentiostatic conditions in a potential window between −0.8 and −1.0 V vs RHE with a signal amplitude 10 mV rms in the frequency range between 100 kHz and 100 mHz. All the experiments were performed after purging the electrolyte with N_2 for 15 min.

Chronopotentiometric experiments were performed under a constant current of 10 mA/cm^2 to study the stability of the HER catalyst and evaluate the H_2 production performance over time. Complementary, hydrogen was detected during chronopotentiometry using a H_2 needle sensor (2.1 × 80 mm) connected to an H2 UniAmp unit (Unisense).

3.3 Computational methods

All structural relaxation calculations were performed using a plane-wave basis set as implemented in the VASP package until the residual forces on atoms were less than 0.03 eV/ Å (Kresse and Furthmüller, 1996). We employed the Projector Augmented Wave (PAW) method to describe the core electrons and the Perdew Burke Ernzerhof exchange-correlation (XC) functional (Perdew et al., 1996; Joubert, 1999). The kinetic energy cut-off for the wave function and charge density was set to 500 eV, and a gamma-point k-grid was used. A vacuum region greater than 10 Å was used to avoid interaction between neighbouring images.

The hydrogen adsorption energy is first calculated as:

$$\Delta E_{H^*} = E_{\text{catalyst+H}^*} - E_{\text{catalyst}} - \tfrac{1}{2}E_{H_2}$$

where, $E_{\text{catalyst+H}^*}$ is the total energy of the catalyst with an H atom attached, E_{catalyst} is the total energy of the same system with no adsorbed hydrogen and E_{H_2} is the energy of a hydrogen molecule in the gas phase. The free energy of hydrogen adsorption is then calculated as $\Delta G_{H^*} = \Delta E_{H^*} + 0.24\,\text{eV}$ eV, to account for the changes in the zero-point energy and the entropy between the adsorbed state and the gas phase of hydrogen.

4 Conclusion

Three new water-reduction molecular electrodes were synthesized utilizing environmentally benign and readily available cobalt containing catalysts, with the idea of producing cost effective and green hydrogen through water reduction at neutral pH. Among these different catalysts' frameworks (porphyrin, phthalocyanine, and corrin) and under the used reaction conditions, the Co-Porphyrin on the modified graphite foil surface showed the best electrocatalytic performance. Molecular level activation due to coordination of the water molecule is anticipated and supported by spectroscopic techniques as the possible reason behind the enhanced activity. Although in homogeneous conditions, Co-Phthalocyanine moiety showed better water reductive current, decreased reactivity after anchoring on the graphite foil surface was observed. This is attributed to the restricted electron transfer due to the spatial orientation and supported by the EIS study. In agreement with the experimental results (e.g., XPS, EIS, Chronopotentiometry), DFT based free energy calculations show better (85 mV lower overpotential) hydrogen production features of Co-Porphyrin than that of the Co-Phthalocyanine moiety.

Data availability statement

The original contributions presented in the study are included in the article/Supplementary Material, further inquiries can be directed to the corresponding author.

Author contributions

ET-C: Data curation, Formal Analysis, Investigation, Visualization, Writing–original draft, Writing–review and editing. MG-R: Data curation, Formal Analysis, Investigation, Validation, Writing–original draft, Writing–review and editing. EM: Formal Analysis, Funding acquisition, Project administration, Resources, Supervision, Writing–original draft, Writing–review and editing. DC-A: Funding acquisition, Project administration, Resources, Supervision, Writing–original draft, Writing–review and editing. FY: Data curation, Formal Analysis, Investigation, Validation, Writing–original draft, Writing–review and editing. VK: Data curation, Formal Analysis, Software, Validation, Writing–original draft, Writing–review and editing. PK: Writing–original draft, Writing–review and editing, Data curation, Formal Analysis, Funding acquisition, Resources, Supervision. OV: Funding acquisition, Writing–original draft, Writing–review and editing. JD: Funding acquisition, Resources, Writing–original draft, Writing–review and editing. BÅ: Funding acquisition, Investigation, Resources, Supervision, Validation, Writing–original draft, Writing–review and editing. BD: Conceptualization, Data curation, Formal Analysis, Funding acquisition, Investigation, Methodology, Project administration, Resources, Supervision, Validation, Visualization, Writing – original draft, Writing – review & editing.

Funding

The author(s) declare that financial support was received for the research, authorship, and/or publication of this article. MG-R thanks Ministerio de Universidades for the FPU20-01746 grant. ET thanks the National Research and Development Agency of Chile - ANID (former CONICYT) for Doctoral scholarship "Beca Chile" 2018-72190682.

Acknowledgments

BD, OV, and BÅ would like to acknowledge research support from the Futura Foundation. VK and PK acknowledge computational support from NCI Australia and Gadi supercomputer. BD acknowledges the computational facilities from Swedish National Infrastructure (SNIC 2020/13-64).

Conflict of interest

The authors declare that the research was conducted in the absence of any commercial or financial relationships that could be construed as a potential conflict of interest.

Publisher's note

All claims expressed in this article are solely those of the authors and do not necessarily represent those of their affiliated organizations, or those of the publisher, the editors and the reviewers. Any product that may be evaluated in this article, or claim that may be made by its manufacturer, is not guaranteed or endorsed by the publisher.

Supplementary material

The Supplementary Material for this article can be found online at: https://www.frontiersin.org/articles/10.3389/fchem.2024.1469804/full#supplementary-material

References

Alemany-Molina, G., Quílez-Bermejo, J., Navlani-García, M., Morallón, E., and Cazorla-Amorós, D. (2022). Efficient and cost-effective ORR electrocatalysts based on low content transition metals highly dispersed on C3N4/super-activated carbon composites. *Carbon* 196, 378–390. doi:10.1016/j.carbon.2022.05.003

Artyushkova, K., Pylypenko, S., Olson, T. S., Fulghum, J. E., and Atanassov, P. (2008). Predictive modeling of electrocatalyst structure based on structure-to-property correlations of X-ray photoelectron spectroscopic and electrochemical measurements. *Langmuir* 24, 9082–9088. doi:10.1021/la801089m

Calabuig-Mompó, S., Cazorla-Amorós, D., and Morallón, E. (2024). Electrocatalysts based on graphene oxide and its buckypaper for enhanced Zn-air battery performance. *J. Electroanal. Chem.* 955, 118069. doi:10.1016/j.jelechem.2024.118069

Cheng, F., Peng, X., Hu, L., Yang, B., Li, Z., Dong, C. L., et al. (2022). Accelerated water activation and stabilized metal-organic framework via constructing triangular active-regions for ampere-level current density hydrogen production. *Nat. Commun.* 13, 6486–6510. doi:10.1038/s41467-022-34278-6

Copéret, C., Chabanas, M., Petroff Saint-Arroman, R., and Basset, J. M. (2003). Surface organometallic chemistry: homogeneous and heterogeneous catalysis: bridging the gap through surface organometallic chemistry. *Angew. Chem. - Int. Ed.* 42, 156–181. doi:10.1002/anie.200390072

Das, B., Thapper, A., Ott, S., and Colbran, S. B. (2019). Structural features of molecular electrocatalysts in multi-electron redox processes for renewable energy – recent advances. *Sustain. Energy Fuels* 3, 2159–2175. doi:10.1039/C9SE00280D

Das, B., Toledo-Carrillo, E. A., Li, G., Ståhle, J., Thersleff, T., Chen, J., et al. (2023). Bifunctional and regenerable molecular electrode for water electrolysis at neutral pH. *J. Mat. Chem. A* 11, 13331–13340. doi:10.1039/d3ta00071k

Das, B., Toledo-Carrillo, E. A., Li, L., Ye, F., Chen, J., Slabon, A., et al. (2022). Cobalt electrocatalyst on fluorine doped carbon cloth – a robust and partially regenerable anode for water oxidation. *ChemCatChem* 14, e202200538. doi:10.1002/cctc.202200538

De Riccardis, A., Lee, M., Kazantsev, R. V., Garza, A. J., Zeng, G., Larson, D. M., et al. (2020). Heterogenized pyridine-substituted cobalt(II) phthalocyanine yields reduction of CO 2 by tuning the electron affinity of the Co center. *ACS Appl. Mat. Interfaces* 12, 5251–5258. doi:10.1021/acsami.9b18924

Elakkiya, R., Ramkumar, R., and Maduraiveeran, G. (2019). Flower-like nickel-cobalt oxide nanomaterials as bi-functional catalyst for electrochemical water splitting. *Mat. Res. Bull.* 116, 98–105. doi:10.1016/j.materresbull.2019.04.016

El-Khouly, M. E., Ito, O., Smith, P. M., and D'Souza, F. (2004). Intermolecular and supramolecular photoinduced electron transfer processes of fullerene-porphyrin/phthalocyanine systems. *J. Photochem. Photobiol. C Photochem. Rev.* 5, 79–104. doi:10.1016/j.jphotochemrev.2004.01.003

Faber, M. S., and Jin, S. (2014). Earth-abundant inorganic electrocatalysts and their nanostructures for energy conversion applications. *Energy Environ. Sci.* 7, 3519–3542. doi:10.1039/C4EE01760A

Giedyk, M., Goliszewska, K., and Gryko, D. (2015). Vitamin B12 catalysed reactions. *Chem. Soc. Rev.* 44, 3391–3404. doi:10.1039/c5cs00165j

Gil-Sepulcre, M., O. Lindner, J., Schindler, D., Velasco, L., Moonshiram, D., Rüdiger, O., et al. (2021). Surface-promoted evolution of Ru-bda coordination oligomers boosts the efficiency of water oxidation molecular anodes. *J. Am. Chem. Soc.* 143, 11651–11661. doi:10.1021/jacs.1c04738

Gong, Y., Zhi, Y., Lin, Y., Zhou, T., Li, J., Jiao, F., et al. (2019). Controlled synthesis of bifunctional particle-like Mo/Mn-Ni x S y/NF electrocatalyst for highly efficient overall water splitting. *Dalt. Trans.* 48, 6718–6729. doi:10.1039/C9DT00957D

Gottfried, M., and Marbach, H. (2009). Surface-confined coordination chemistry with porphyrins and phthalocyanines: aspects of formation, electronic structure, and reactivity. *Z. für Phys. Chem.* 223, 53–74. doi:10.1524/zpch.2009.6024

Gupta, S., Fernandes, R., Patel, R., Spreitzer, M., and Patel, N. (2023). A review of cobalt-based catalysts for sustainable energy and environmental applications. *Appl. Catal. A Gen.* 661, 119254. doi:10.1016/j.apcata.2023.119254

Hoque, M. A., Gil-Sepulcre, M., de Aguirre, A., Elemans, J. A. A. W., Moonshiram, D., Matheu, R., et al. (2020). Water oxidation electrocatalysis using ruthenium coordination oligomers adsorbed on multiwalled carbon nanotubes. *Nat. Chem.* 12, 1060–1066. doi:10.1038/s41557-020-0548-7

Hu, K., Wu, M., Hinokuma, S., Ohto, T., Wakisaka, M., Fujita, J., et al. (2019). Boosting electrochemical water splitting via ternary NiMoCo hybrid nanowire arrays. *J. Mat. Chem. A* 7, 2156–2164. doi:10.1039/C8TA11250A

Jia, C., Ching, K., V. Kumar, P., Zhao, C., Kumar, N., Chen, X., et al. (2020). Vitamin B12 on graphene for highly efficient CO_2 electroreduction. *ACS Appl. Mat. and Interfaces* 12, 41288–41293. doi:10.1021/acsami.0c10125

Joubert, D. (1999). From ultrasoft pseudopotentials to the projector augmented-wave method. *Phys. Rev. B - Condens. Matter Mat. Phys.* 59, 1758–1775. doi:10.1103/PhysRevB.59.1758

Ju, W., Bagger, A., Hao, G. P., Varela, A. S., Sinev, I., Bon, V., et al. (2017). Understanding activity and selectivity of metal-nitrogen-doped carbon catalysts for electrochemical reduction of CO_2. *Nat. Commun.* 8, 944–949. doi:10.1038/s41467-017-01035-z

Kandemir, B., Kubie, L., Guo, Y., Sheldon, B., and Bren, K. L. (2016). Hydrogen evolution from water under aerobic conditions catalyzed by a cobalt ATCUN metallopeptide. *Inorg. Chem.* 55, 1355–1357. doi:10.1021/acs.inorgchem.5b02157

Kärkäs, M. D., Verho, O., Johnston, E. V., and Åkermark, B. (2014). Artificial photosynthesis: molecular systems for catalytic water oxidation. *Chem. Rev.* 114, 11863–12001. doi:10.1021/CR400572F

Kim, H., Park, J., Park, I., Jin, K., Jerng, S. E., Kim, S. H., et al. (2015). Coordination tuning of cobalt phosphates towards efficient water oxidation catalyst. *Nat. Commun.* 6, 8253. doi:10.1038/ncomms9253

Kresse, G., and Furthmüller, J. (1996). Efficient iterative schemes for *ab initio* total-energy calculations using a plane-wave basis set. *Phys. Rev. B - Condens. Matter Mat. Phys.* 54, 11169–11186. doi:10.1103/PhysRevB.54.11169

Lee, K. J., McCarthy, B. D., and Dempsey, J. L. (2019). On decomposition, degradation, and voltammetric deviation: the electrochemist's field guide to identifying precatalyst transformation. *Chem. Soc. Rev.* 48, 2927–2945. doi:10.1039/c8cs00851e

Li, F., Han, G. F., Noh, H. J., Jeon, J. P., Ahmad, I., Chen, S., et al. (2019a). Balancing hydrogen adsorption/desorption by orbital modulation for efficient hydrogen evolution catalysis. *Nat. Commun.* 10, 4060–4067. doi:10.1038/s41467-019-12012-z

Li, M., Zhu, Y., Wang, H., Wang, C., Pinna, N., and Lu, X. (2019b). Ni strongly coupled with Mo_2C encapsulated in nitrogen-doped carbon nanofibers as robust bifunctional catalyst for overall water splitting. *Adv. Energy Mat.* 9, 1803185. doi:10.1002/aenm.201803185

Li, R., Li, X., Yu, D., Li, L., Yang, G., Zhang, K., et al. (2019c). $Ni_3ZnC_{0.7}$ nanodots decorating nitrogen-doped carbon nanotube arrays as a self-standing bifunctional electrocatalyst for water splitting. *Carbon* 148, 496–503. doi:10.1016/j.carbon.2019.04.002

Macquet, J. P., Millard, M. M., and Theophanides, T. (1978). X-ray photoelectron spectroscopy of porphyrins. *J. Am. Chem. Soc.* 100, 4741–4746. doi:10.1021/ja00483a018

Mahmood, N., Yao, Y., Zhang, J. W., Pan, L., Zhang, X., and Zou, J. J. (2018). Electrocatalysts for hydrogen evolution in alkaline electrolytes: mechanisms, challenges, and prospective solutions. *Adv. Sci.* 5, 1700464. doi:10.1002/advs.201700464

Makhado, T., Das, B., Kriek, R. J., Vosloo, H. C. M., and Swarts, A. J. (2021). Chemical and electrochemical water oxidation mediated by bis(pyrazol-1-ylmethyl)pyridine-ligated Cu(i) complexes. *Sustain. Energy Fuels* 5, 2771–2780. doi:10.1039/d1se00402f

McAlpin, J. G., Surendranath, Y., Dincă, M., Stich, T. A., Stoian, S. A., Casey, W. H., et al. (2010). EPR evidence for Co(IV) species produced during water oxidation at neutral pH. *J. Am. Chem. Soc.* 132, 6882–6883. doi:10.1021/ja1013344

Mette, G., Sutter, D., Gurdal, Y., Schnidrig, S., Probst, B., Iannuzzi, M., et al. (2016). From porphyrins to pyrphyrins: adsorption study and metalation of a molecular catalyst on Au(111). *Nanoscale* 8, 7958–7968. doi:10.1039/C5NR08953K

Moni, P., Hyun, S., Vignesh, A., and Shanmugam, S. (2017). Chrysanthemum flower-like $NiCo_2O_4$–nitrogen doped graphene oxide composite: an efficient electrocatalyst for lithium–oxygen and zinc–air batteries. *Chem. Commun.* 53, 7836–7839. doi:10.1039/C7CC03826G

Okamoto, Y., Nakano, H., Imanaka, T., and Teranishi, S. (1975). X-ray photoelectron spectroscopic studies of catalysts — supported cobalt catalysts —. *Bull. Chem. Soc. Jpn.* 48, 1163–1168. doi:10.1246/bcsj.48.1163

Peebles, C., He, M., Feng, Z., Su, C.-C., Zeng, L., Bedzyk, M. J., et al. (2017). Investigation of glutaric anhydride as an electrolyte additive for graphite/$LiNi_{0.5}Mn_{0.3}Co_{0.2}O_2$ full cells. *J. Electrochem. Soc.* 164, A173–A179. doi:10.1149/2.0721702jes

Perdew, J. P., Burke, K., and Ernzerhof, M. (1996). Generalized gradient approximation made simple. *Phys. Rev. Lett.* 77, 3865–3868. doi:10.1103/PhysRevLett.77.3865

Petraki, F., Peisert, H., Biswas, I., and Chassé, T. (2010). Electronic structure of Co-phthalocyanine on gold investigated by photoexcited electron spectroscopies: indication of Co Ion–Metal interaction. *J. Phys. Chem. C* 114, 17638–17643. doi:10.1021/jp104141s

Saravanan, N., Balamurugan, M., Shalini Devi, K. S., Nam, K. T., and Senthil Kumar, A. (2020). Vitamin B12-immobilized graphene oxide for efficient electrocatalytic carbon dioxide reduction reaction. *ChemSusChem* 13, 5620–5624. doi:10.1002/cssc.202001378

Schmid, M., Kaftan, A., Steinrück, H.-P., and Gottfried, J. M. (2012). The electronic structure of cobalt(II) phthalocyanine adsorbed on Ag(111). *Surf. Sci.* 606, 945–949. doi:10.1016/j.susc.2012.02.012

Shiva Kumar, S., and Lim, H. (2022). An overview of water electrolysis technologies for green hydrogen production. *Energy Rep.* 8, 13793–13813. doi:10.1016/j.egyr.2022.10.127

Sun, H., Smirnov, V. V., and DiMagno, S. G. (2003). Slow electron transfer rates for fluorinated cobalt porphyrins: electronic and conformational factors modulating metalloporphyrin ET. *Inorg. Chem.* 42, 6032–6040. doi:10.1021/ic034705o

Sun, W., Wang, Y., Wu, H., Wang, Z., Rooney, D., and Sun, K. (2017). 3D free-standing hierarchical $CuCo_2O_4$ nanowire cathodes for rechargeable lithium–oxygen batteries. *Chem. Commun.* 53, 8711–8714. doi:10.1039/C7CC02621H

Sun, Y., Zhang, T., Li, C., Xu, K., and Li, Y. (2020). Compositional engineering of sulfides, phosphides, carbides, nitrides, oxides, and hydroxides for water splitting. *J. Mat. Chem. A* 8, 13415–13436. doi:10.1039/D0TA05038E

Toledo-Carrillo, E. A., García-Rodríguez, M., Sánchez-Moren, L. M., and Dutta, J. (2024). Decoupled supercapacitive electrolyzer for membrane-free water splitting. *Sci. Adv.* 10, eadi3180. doi:10.1126/sciadv.adi3180

Ventosa, M., Gil-Sepulcre, M., Benet-Buchholz, J., Gimbert-Suriñach, C., and Llobet, A. (2021). Anode based on a molecular Ru water oxidation catalyst covalently bonded to polythiophene. *ACS Appl. Energy Mat.* 4, 9775–9782. doi:10.1021/acsaem.1c01851

Wang, J., Yue, X., Yang, Y., Sirisomboonchai, S., Wang, P., Ma, X., et al. (2020). Earth-abundant transition-metal-based bifunctional catalysts for overall electrochemical water splitting: a review. *J. Alloys Compd.* 819, 153346. doi:10.1016/j.jallcom.2019.153346

Xie, X., Song, M., Wang, L., Engelhard, M. H., Luo, L., Miller, A., et al. (2019). Electrocatalytic hydrogen evolution in neutral pH solutions: dual-phase synergy. *ACS Catal.* 9, 8712–8718. doi:10.1021/acscatal.9b02609

Xu, Y., Yan, Y., He, T., Zhan, K., Yang, J., Zhao, B., et al. (2019). Supercritical CO_2-Assisted synthesis of $NiFe_2O_4$/vertically-aligned carbon nanotube arrays hybrid as a bifunctional electrocatalyst for efficient overall water splitting. *Carbon* 145, 201–208. doi:10.1016/j.carbon.2019.01.011

Yanagiya, S. I., Wakamatsu, H., Nishikata, O., and Inoue, T. (2004). Growth of cobalt-phthalocyanine on KCl (001) substrate and copper-phthalocyanine whisker. *Jpn. J. Appl. Phys.* 43, 7722–7724. doi:10.1143/JJAP.43.7722

Yang, L., Liu, D., Hao, S., Kong, R., Asiri, A. M., Zhang, C., et al. (2017). A cobalt-borate nanosheet array: an efficient and durable non-noble-metal electrocatalyst for water oxidation at near neutral pH. *J. Mat. Chem. A* 5, 7305–7308. doi:10.1039/c7ta00982h

Zagal, J., Páez, M., Tanaka, A. A., dos Santos, J. R., and Linkous, C. A. (1992). Electrocatalytic activity of metal phthalocyanines for oxygen reduction. *J. Electroanal. Chem.* 339, 13–30. doi:10.1016/0022-0728(92)80442-7

Zainal, B. S., Ker, P. J., Mohamed, H., Ong, H. C., Fattah, I. M. R., Rahman, S. M. A., et al. (2024). Recent advancement and assessment of green hydrogen production technologies. *Renew. Sustain. Energy Rev.* 189, 113941. doi:10.1016/j.rser.2023.113941

Zhang, B., Zhang, X., Wei, Y., Xia, L., Pi, C., Song, H., et al. (2019). General synthesis of NiCo alloy nanochain arrays with thin oxide coating: a highly efficient bifunctional electrocatalyst for overall water splitting. *J. Alloys Compd.* 797, 1216–1223. doi:10.1016/j.jallcom.2019.05.036

Zhang, J., My Pham, T. H., Gao, Z., Li, M., Ko, Y., Lombardo, L., et al. (2023). Electrochemical CO_2 reduction over copper phthalocyanine derived catalysts with enhanced selectivity for multicarbon products. *ACS Catal.* 13, 9326–9335. doi:10.1021/acscatal.3c01439

Zhang, Z., and Wang, Y. G. (2021). Molecular design of dispersed nickel Phthalocyanine@Nanocarbon hybrid catalyst for active and stable electroreduction of CO_2. *J. Phys. Chem. C* 125, 13836–13849. doi:10.1021/acs.jpcc.1c02508

Zhu, F., Liu, Y., Yan, M., and Shi, W. (2018). Construction of hierarchical $FeCo_2O_4$@MnO_2 core-shell nanostructures on carbon fibers for high-performance asymmetric supercapacitor. *J. Colloid Interface Sci.* 512, 419–427. doi:10.1016/j.jcis.2017.09.093

Zhu, M., Shao, Q., Qian, Y., and Huang, X. (2019). Superior overall water splitting electrocatalysis in acidic conditions enabled by bimetallic Ir-Ag nanotubes. *Nano Energy* 56, 330–337. doi:10.1016/j.nanoen.2018.11.023